nature methods

ARTICLES

https://doi.org/10.1038/s41592-018-0143-7

Fast and accurate data collection for macromolecular crystallography using the JUNGFRAU detector

Filip Leonarski[1], Sophie Redford[1], Aldo Mozzanica[1], Carlos Lopez-Cuenca[1], Ezequiel Panepucci[1], Karol Nass[1], Dmitry Ozerov[1], Laura Vera[1], Vincent Olieric[1], Dominik Buntschu[1], Roman Schneider[1], Gemma Tinti[1], Erik Froejdh[1], Kay Diederichs[2], Oliver Bunk[1], Bernd Schmitt[1]* and Meitian Wang[1]*

The accuracy of X-ray diffraction data is directly related to how the X-ray detector records photons. Here we describe the application of a direct-detection charge-integrating pixel-array detector (JUNGFRAU) in macromolecular crystallography (MX). JUNGFRAU features a uniform response on the subpixel level, linear behavior toward high photon rates, and low-noise performance across the whole dynamic range. We demonstrate that these features allow accurate MX data to be recorded at unprecedented speed. We also demonstrate improvements over previous-generation detectors in terms of data quality, using native single-wavelength anomalous diffraction (SAD) phasing, for thaumatin, lysozyme, and aminopeptidase N. Our results suggest that the JUNGFRAU detector will substantially improve the performance of synchrotron MX beamlines and equip them for future synchrotron light sources.

MX reveals 3D structures and elucidates functions of biomolecules with atomic resolution, thereby enabling researchers to make fundamental contributions to molecular biology and structure-based drug discovery[1]. Synchrotron radiation, together with large-format 2D detectors, has been essential to the success of modern MX[2,3]. In parallel with the evolution of synchrotron sources, several generations of X-ray detectors have been developed, namely, image plates[4], multiwire proportional counters[5], X-ray television detectors[6], charge-coupled device (CCD) detectors[7], and hybrid (pixel-array) photon-counting (HPC) detectors[8]. Currently, most MX beamlines are equipped with HPC detectors, or are scheduled to be.

Each new generation of X-ray detector has transformed MX data-collection strategies. The traditional high-dose and coarse-phi slicing data-collection strategy adapted for CCD detectors[9,10] has been replaced by a continuous, low-dose and fine-phi slicing strategy that takes full advantage of HPC detectors[11,12]. Very recently, the EIGER detector[13,14] enabled new data-collection protocols that incorporate fast raster scanning[15] and serial crystallography[16].

Some of the key features of HPC detectors are very low-noise detection and a point-spread response of a single pixel, achieved by counting of an incoming photon only in the pixel where it deposits at least 50% of its energy. Thus, photon counters have negligible readout noise, which means that the accuracy of their measurements is limited by their calibration, systematic effects, and Poisson statistics.

However, there are two intrinsic effects that may lead to photons going undetected by photon-counting devices, namely, charge-sharing and pileup. Charge-sharing results in spreading of photon-induced charges into adjacent pixels when photons hit the sensor near the pixel border ('corner effect'). In such situations, the detection (counting) of the photons strongly depends on the threshold settings. The calibration of the threshold becomes less accurate at low photon energies (≤8 keV), and a 50% threshold might not be achievable. Therefore, the effects could be detrimental in low-energy applications such as native-SAD phasing, where highly accurate measurement of intensity is needed. The effect could be mitigated to a certain degree by an increase in the pixel size (for example, 170 µm pitch in the PILATUS[11]) or by a charge-summing and allocation method as implemented in MEDIPIX3[17], but such measures reduce spatial resolution and count-rate capability.

Pileup effects occur at high photon rates as a result of the dead time in the readout electronic circuit, which needs some time to reset before the next photon can be detected. This count-rate dependence of HPC detectors leads to a nonlinear response to photon flux, necessitating a count-rate correction[18]. A recent development in retriggering technology[19] extends the count-rate capacity of HPC detectors but does not eliminate the problem. As an added complication, the count-rate correction in its simplest form is valid only with a constant flux of photons. However, in practice no count-rate correction is applied for a changing photon rate when a sharp Bragg peak moves through the diffraction condition during a single exposure. These count-rate-related issues are usually avoided in MX measurements, which are carried out with an attenuated beam at a low rotation speed. However, the count-rate capability will become acute for the next-generation synchrotrons with higher brilliance[20,21].

A challenge in detector development is finding a way to overcome the aforementioned charge-sharing and pileup effects while maintaining low-noise performance at the single-photon level and with a high dynamic range. New charge-integrating hybrid pixel detectors could meet such challenges[22,23]; JUNGFRAU is one example[24]. Initially developed for X-ray free-electron laser (XFEL) applications[25], JUNGFRAU features direct detection and dynamic gain-switching technology[24]. Instead of counting individual photons by using a threshold, JUNGFRAU measures the total amount

[1]Swiss Light Source, Paul Scherrer Institute, Villigen, Switzerland. [2]Fachbereich Biologie, Universität Konstanz, Konstanz, Germany.
*e-mail: bernd.schmitt@psi.ch; meitian.wang@psi.ch

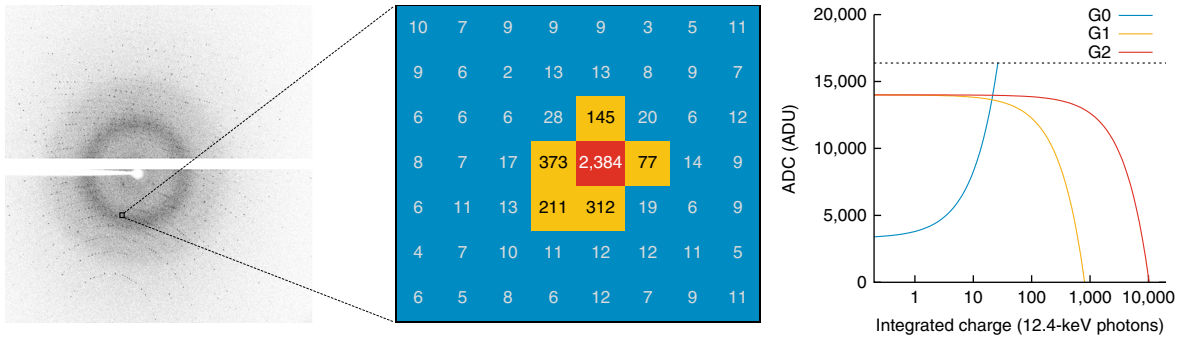

Fig. 1 | Demonstration of the dynamic gain-switching of the JUNGFRAU detector. Left: a diffraction image from a lysozyme crystal measured without beam attenuation at the X06SA beamline, Swiss Light Source. Middle: zoomed-in view of a Bragg peak showing the number of photons detected, where the central pixel was measured in low gain (red), tails of the peak were measured in medium gain (yellow), and the background was measured in high gain (blue). Right: the relationship between a charge integrated by the pixel and its analog-to-digital converter (ADC) count output for three gains (high (G0), medium (G1), and low (G2)) in analog-to-digital converter units (ADU). The dashed line represents the highest count permitted by a 14-bit ADC: $2^{14} - 1 = 16{,}383$.

of charge accumulated during the integration time, by which it entirely eliminates both the charge-sharing problem and the count-rate limitation. As shown in Fig. 1, the JUNGFRAU has three separate gains per pixel, which means that low-intensity regions of the frame benefit from high gain and single-photon sensitivity, whereas strongly diffracting Bragg peaks are accurately measured thanks to the ability to switch to low gain and extend the dynamic range to 12 million counts per second (Mcps) per pixel at 12.0 keV, limited by the current 1.1-kHz frame rate[26]. The gain is switched automatically and independently per pixel depending on the detected charge. The result of this approach is the combination of a linear response up to much higher photon rates and noise well below the limits set by Poisson counting statistics. We illustrate this for one recorded Bragg peak from a lysozyme crystal in Fig. 1.

Here we demonstrate that JUNGFRAU maintains the advantages of HPC detectors for routine MX applications and offers considerable improvements in data acquisition speed and low-energy phasing.

Results

JUNGFRAU maintains low-noise performance. The reliable detection of high-resolution weak reflections is the foremost requirement for X-ray detectors in MX. In this aspect, HPC detectors are nearly ideal because of their very low-noise detection with single-photon sensitivity and single-pixel point-spread function. We compared JUNGFRAU's low-noise performance with that of EIGER, a widely used HPC detector, in the most common MX application: native data collection with 12.4-keV X-rays. These two detectors are particularly suited to a comparison of photon-counting versus charge-integrating methods because they have the same pixel size, same sensor area, same hybrid nature, and similar sensor thickness. We collected two datasets with the same thaumatin crystal under identical X-ray beam conditions (Methods): one with a JUNGFRAU 1-megapixel detector (JF1M; Supplementary Fig. 1), and the other with an EIGER 1-megapixel detector (E1M). We deliberately set the dose very low (0.6 kGy per dataset) to have Poisson-statistics-limited noise for the whole resolution range.

The two datasets had almost the same quality, with similar values of equivalent reflection agreement indicator R_{meas} (Fig. 2a, Supplementary Tables 1 and 2). Both detectors recorded very weak intensities down to the one-photon level at resolutions of 2 Å and higher. The half-dataset correlations ($CC_{1/2}$), mean intensities, and mean signal-to-noise ratio of unmerged reflections ($\langle I/\sigma \rangle_{unmrgd}$) were marginally lower for JF1M because of its slightly reduced duty cycle and thinner Si sensor (Fig. 2b–d). After normalization for detector duty cycle (JF1M 95% versus E1M 99.7%) and sensor thickness (JF1M 320 µm versus E1M 450 µm) (Methods), the intensities and

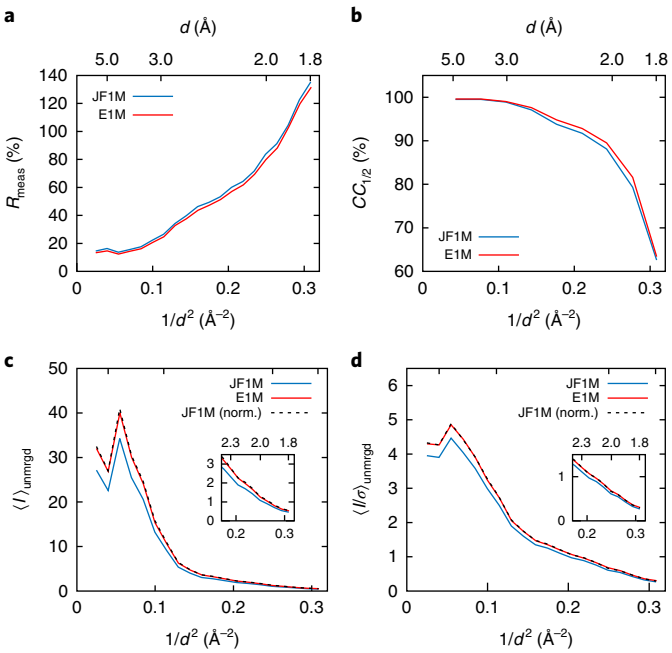

Fig. 2 | Comparison of data quality between JF1M and E1M data from routine MX applications. All comparisons are made as a function of resolution (d). **a**, R_{meas} values. **b**, $CC_{1/2}$ values. **c**, The intensity ($\langle I \rangle_{unmrgd}$) values with and without normalization (norm.) for the duty cycle and sensor thickness. The $\langle I \rangle_{unmrgd}$ values represent values before application of Lorentz and polarization corrections. **d**, $\langle I/\sigma \rangle_{unmrgd}$ values. Insets in **c**,**d** show expanded views for the high-resolution range.

$\langle I/\sigma \rangle_{unmrgd}$ values were virtually the same in the whole resolution range for both detectors (Fig. 2c,d). As the maximum duty cycle of JUNGFRAU will be improved to the 99% level in the future, and as thicker sensors may be chosen during detector construction, it is expected that the performance of JUNGFRAU will approach the excellent results of EIGER for weak diffraction.

JUNGFRAU enables data collection with full flux. To test JUNGFRAU for high-count-rate applications, we conducted a series of experiments with increasing flux (beam transmission: 1%, 20%, 50%, and 100%) and rotation speed (1°, 20°, 50°, and 100° s^{-1}) using a thaumatin crystal at 6 keV (Methods). Compared with published results of similar experiments with an E1M detector, in which

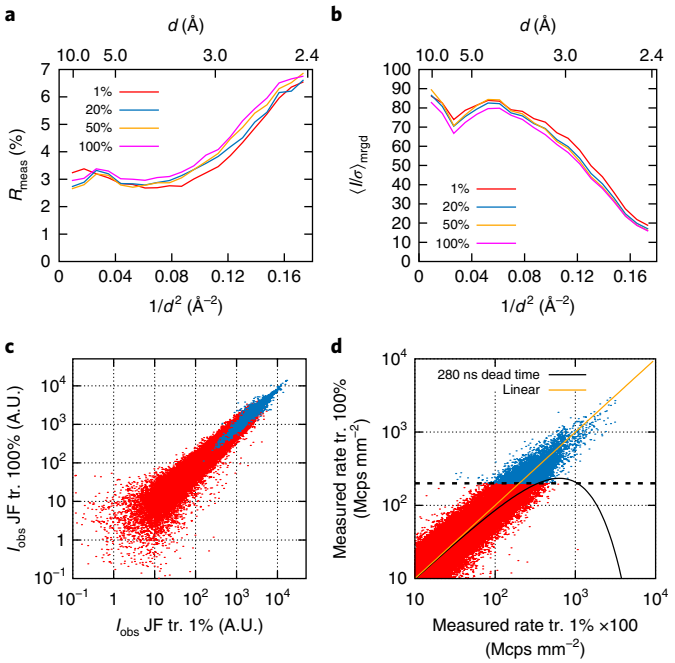

Fig. 3 | Comparison of measurements with different photon rates acquired with the JUNGFRAU detector. a,**b**, The (**a**) R_{meas} and (**b**) $\langle I/\sigma \rangle_{mrgd}$ values for measurements obtained with beam transmissions at 1%, 20%, 50%, and 100%. **c**, The correlation of integrated intensities of reflections measured with beam transmission (tr.) of 100% with respective intensities measured at 1% transmission (Pearson correlation coefficient of 0.98). Red and blue dots represent reflections with photon rates below and above 200 Mcps mm^{-2}, respectively. A.U., arbitrary units. **d**, The correlation of the estimated photon rate extracted from the single pixel of a reflection with the highest counts between the 1% and 100% transmission datasets (Pearson correlation coefficient of 0.93). The spread of the plot comes from the fact that depending on the slicing position of a reflection, the number of photons might differ for the pixel with the highest counts. The orange line represents an ideal linear response. The black curve is the theoretical behavior of a paralyzable counter with a dead time of 280 ns, and the horizontal dashed black line marks a corresponding count-rate limit.

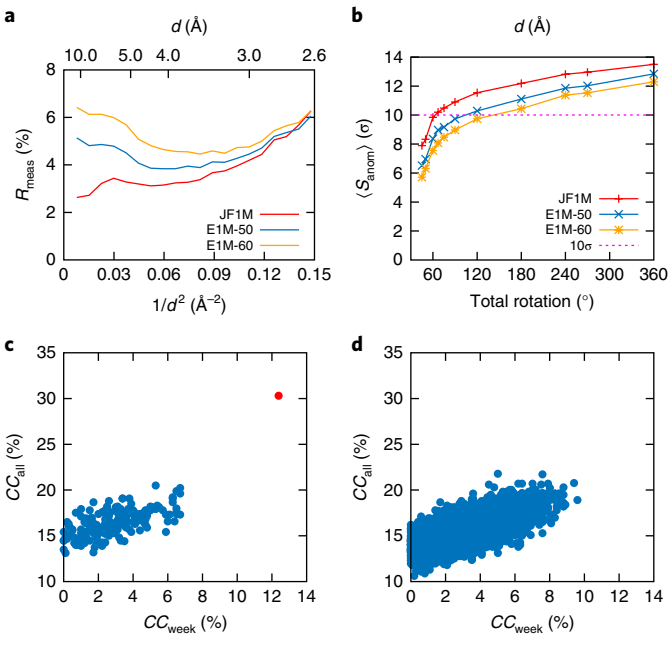

Fig. 4 | Comparison of 6-keV thaumatin crystal data measured with JF1M and E1M detectors (two threshold settings for E1M). a, The crystallographic R_{meas} as a function of resolution. **b**, The anomalous signal ($\langle S_{anom} \rangle$) as a function of total rotation range. The dashed magenta line represents the threshold for structure solvability. **c**, SHELXD substructure determination from 200 trials with 60° JF1M data. The correct solution with high CC_{all} and high CC_{weak} is indicated by a red dot. **d**, SHELXD substructure determination from 5,000 trials with 60° E1M-50 data.

the data quality gradually deteriorated with increased flux owing to the count-rate limit[14], the four JF1M datasets were of very similar quality as judged by R_{meas} and $\langle I/\sigma \rangle$ (Fig. 3a,b, Supplementary Tables 1 and 3), and their intensity correlations were in excellent agreement across the whole dynamic range (Fig. 3c). In the JF1M 100° s^{-1} dataset, the top first and sixth percentiles of strong reflections contained data recorded with photon rates of 500 and 200 Mcps mm^{-2}, respectively (Methods, Supplementary Table 4), which are beyond and close to the count-rate limit of typical HPC detectors, respectively. The strongest reflection in the dataset ($h=1, k=1, l=1$) showed that JUNGFRAU operated at 1.136 kHz is capable of measuring photon rates of more than 4,300 Mcps mm^{-2} at an X-ray energy of 6 keV (Fig. 3d).

JUNGFRAU improves data accuracy. We performed a native-SAD phasing experiment to assess the quality of data obtained with the JUNGFRAU detector, because this method relies on very accurate measurements of reflection intensities to derive phases[27,28]. We measured a thaumatin crystal with 6-keV X-rays using the JF1M and E1M detectors (Methods). We used two settings for E1M: one with the default 50% threshold (E1M-50), and the other with a 60% threshold (E1M-60) to simulate a situation in which the lowest possible threshold is higher than 50% of the photon energy (<6 keV). For the direct comparison, all measurements were made at the same position of the same crystal with identical data-collection parameters (Methods). For this thaumatin crystal, the typical size of a diffraction spot was a few pixels on average and was smaller at low resolution than at high resolution because of the parallax in the diffraction geometry (Supplementary Fig. 2).

The recorded JF1M data were of high quality as evaluated by R_{meas} (Fig. 4a, Supplementary Tables 1 and 5) and $\langle I/\sigma \rangle$ (Supplementary Fig. 3). The R_{meas} of 2.5% measured at the lowest-resolution shell reflects the excellent consistency between individual measurements. R_{meas} gradually increased with the resolution to 5% at 2.7 Å, with a characteristic bump around 6 Å due to an intensity distribution typical of most protein crystals. In contrast, the E1M-50 data were noticeably worse at low resolution, with R_{meas} of 5%. The data quality deteriorated further in the E1M-60 data. Such differences had a considerable effect on the average density in the anomalous difference Fourier map for sulfur atoms ($\langle S_{anom} \rangle$; Fig. 4b). $\langle S_{anom} \rangle$ is a useful metric for structure solvability in SAD phasing, and a value greater than 10σ usually indicates sufficient signal for structure solution[29]. We obtained $\langle S_{anom} \rangle$ values of 10.2σ, 8.9σ, and 8.3σ for 75° with JF1M, E1M-50, and E1M-60, respectively. Two to three times more data were required to elevate $\langle S_{anom} \rangle$ above 10σ for E1M data (Fig. 4b). Indeed, the substructure was solved with SHELXC/D[30] with merely 60° JF1M data (Fig. 4c), whereas the same 60° data from E1M-50 did not produce a structure solution (Fig. 4d).

To understand the origin of the discrepancy in quality between data obtained with JF1M and that obtained with E1M, we quantified the uniform response at the sub-pixel level by mapping the deviation of intensities in fractional coordinates of 1 pixel on the basis of the refined position of reflections ($\Delta_{x,y}$). Then we calculated an average pixel map with the normalized $\Delta_{x,y}$ (Methods; equation (4)). In the case of JF1M the pixel map was essentially

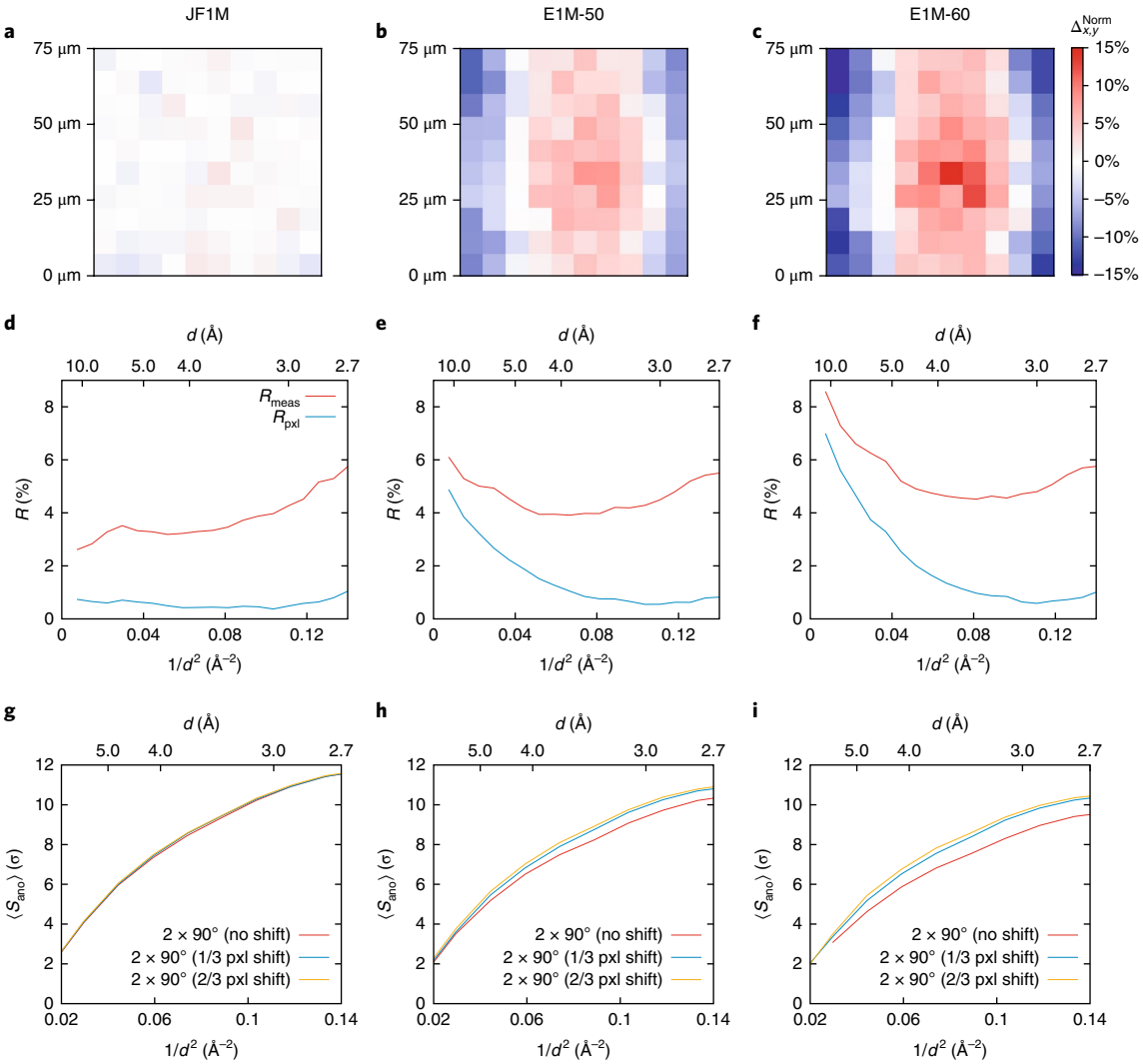

Fig. 5 | Sub-pixel uniformity characterization of the JUNGFRAU and EIGER detectors. Data are shown for JF1M (**a**,**d**,**g**), E1M-50 (**b**,**e**,**h**), and E1M-60 (**c**,**f**,**i**). **a**–**c**, Pixel maps for low-resolution data (>10 Å) (equation (4), Methods). **d**–**f**, R_{pxl} (equation (5), Methods) and crystallographic R_{meas} as a function of resolution. **g**–**i**, Measured anomalous signals from combined datasets with and without detector shifts. Reflections flagged as misfit by XDS software were included in calculations of the statistics.

featureless, indicating no significant bias in intensity measurement regardless of where the reflection was located within the pixel (Fig. 5a), as expected for a charge-integrating detector. However, in the case of E1M-50 there was a systematic difference between reflections centered in the middle of a pixel and those near the corners (Fig. 5b), and the magnitude of the effect increased with the detector threshold (Fig. 5c). Because most diffraction spots of the crystal were elongated in the vertical direction (Supplementary Fig. 2), the effect was much stronger in the horizontal direction in the E1M pixel maps. It is likely that the nonuniformity in EIGER can be attributed to this corner effect, inaccuracy in threshold calibration, and count-rate corrections at low energy. To estimate the contribution of these effects to crystallographic R_{meas}, we introduced R_{pxl} as a measure of systematic errors caused by the nonuniformity across pixels by averaging out random errors (Methods; equation (5)). R_{pxl} values were <1% for JF1M (Fig. 5d). For E1M data, R_{pxl} had a resolution-dependent behavior because the detector nonuniformity was more visible for sharp low-resolution spots. It increased gradually from 3 Å toward lower resolution and became a main contributor to the higher R_{meas} in the low-resolution range (Fig. 5e,f).

We also verified the sub-pixel and inter-pixel uniformity in JF1M by means of detector-shifting experiments in which we measured datasets with JF1M shifted by one-third and two-thirds of a pixel in a diagonal direction orthogonal to the beam direction. When we combined two datasets—one with and one without the JF1M shift—we achieved a data accuracy equal to that measured with the same amount of data collected with only one detector position (Fig. 5g). In similar detector-shift experiments with E1M, the data accuracy improved substantially when we combined data from two detector positions to average out the nonuniform response within and between pixels with E1M (Fig. 5h,i). This analysis confirms that JUNGFRAU has good uniform responses within pixels, which permits the measurement of reflection intensities with high accuracy even at low X-ray energies and with diffraction peak sizes similar to the size of the pixel.

JUNGFRAU expedites experimental phasing. Accurate measurement of reflection intensities with high incoming photon rates, made possible by JUNGFRAU, enables efficient use of the full flux provided by an undulator beamline for experimental phasing with anomalous diffraction, the success of which stringently depends on the data accuracy. We chose one of the most challenging phasing methods—native SAD—to demonstrate JUNGFRAU's distinct advantages.

First, we demonstrated that a flash of low-energy X-rays less than 1 s in duration is sufficient for native-SAD phasing with a thaumatin

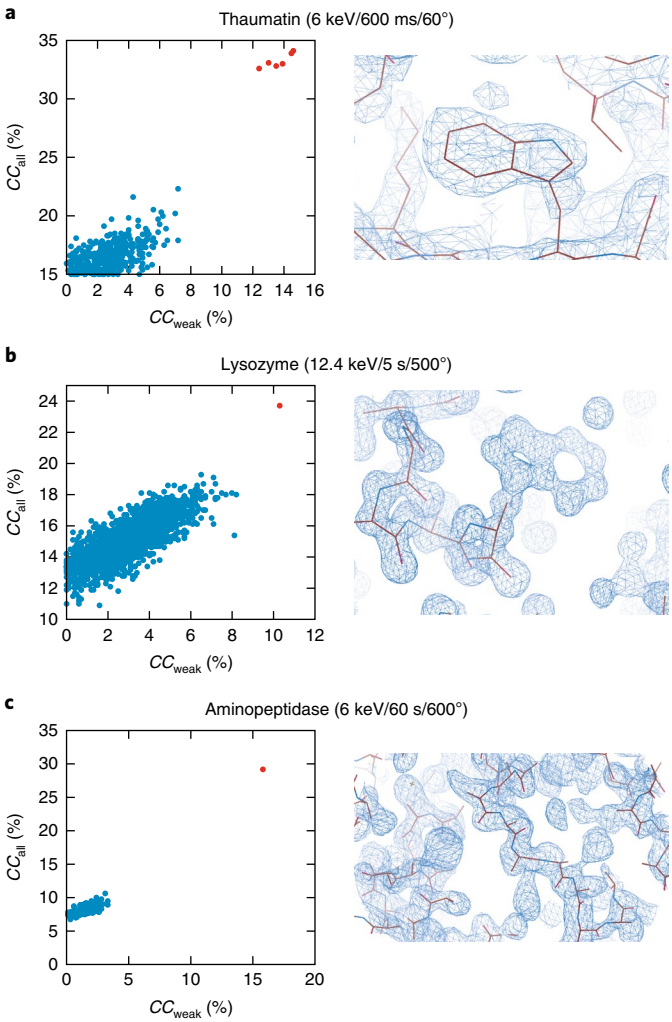

Fig. 6 | Fast native-SAD phasing with an unattenuated beam at both 6 keV and 12.4 keV with JF1M. For each case, results of the substructure search with SHELXD are shown on the left, with the correct solutions with high CC_{all} and high CC_{weak} marked as red dots, and the electron density map is shown on the right. **a**, Thaumatin with 60° of data measured in 600 ms at 6 keV. Density map obtained after density modification, automated tracing, and refinement with CRANK2. **b**, Lysozyme with 500° of data measured in 5 s at 12.4 keV. Density map obtained after density modification and automated tracing with SHELXE. **c**, PepN with 600° of data measured in 1 min at 6 keV. Density map obtained after density modification and automated tracing with SHELXE.

crystal as the model system. We collected a total of 60° of data from one crystal at 6 keV with a rotation speed of 100° s^{-1}. The entire exposure lasted 0.6 s. With these data, all sulfurs were identified readily with SHELXD[30], and the resulting electron density map from CRANK2[31] was of excellent quality (Fig. 6a). The multiplicity of the dataset was only 2.1 (Supplementary Tables 1 and 6). This illustrates that the uniform response of JUNGFRAU achieves high data accuracy with minimum averaging.

To probe the limit further, we attempted a native-SAD experiment with 12.4-keV X-rays using a lysozyme crystal. This energy is unfavorable for a native-SAD experiment because the anomalous scattering factor f'' of sulfur is only 0.24 e^-. Although the estimated average difference in structure factors of Friedel pairs (i.e., Bijvoet ratio) was as low as 0.6%, the structure was phased by SHELXC/D/E with a 500° dataset measured in only 5 s (Fig. 6b). In this case, high-resolution data up to 1.15 Å also contributed to the accumulation of weak anomalous signals (Supplementary Tables 1 and 6).

Next, we selected *Escherichia coli* aminopeptidase N (PepN), representing a more challenging example. PepN is a 101-kDa protein (891 residues) containing 30 sulfurs, 1 bromine, and 1 zinc atom. Because the average diffraction power of PepN is much weaker than that of test proteins such as thaumatin and lysozyme, we limited the rotation speed of data collection to 10° s^{-1} to ensure sufficient exposure per diffraction image with a flux of 2.7×10^{11} photons per second at 6 keV. A 600° dataset, collected in 1 min (Supplementary Tables 1 and 6), allowed a straightforward structure solution using SHELXC/D/E (Fig. 6c). If five to ten times more flux were available, we would expect that the same structure could be solved within 5–10 s using 50–100° s^{-1} rotation.

Discussion

The diffraction pattern of a macromolecular crystal contains thousands of sharp Bragg peaks with large variations in intensity. Structure solution, especially by experimental phasing methods, requires accurate measurement of strong Bragg peaks, and the atomic features of a structure are determined by precise recording of weak Bragg peaks at high resolution. Strong and weak intensities pose different challenges for measurement. Ideally a detector should have a uniform response across a large surface area on both the pixel and the sub-pixel level, a high dynamic range with a linear response, high sensitivity to the single-photon level, a single-pixel point-spread function, and continuous readout. None of the previous generations of detectors addressed all of these points. JUNGFRAU meets the challenge by using a charge-integrating readout chip and direct-detection hybrid pixel detector technology to provide a low-noise performance over the whole dynamic range of 10^4 12-keV photons per frame per pixel and a uniform response within and across pixels.

From a data accuracy and precision point of view, the requirements are most stringent in experimental phasing because the small anomalous differences (≤1%) between Bragg peaks related by Friedel's law and crystal symmetry lead to reliable evaluation of phases. If the size of Bragg spots is similar to or smaller than the pixel size of the detector, their measurement accuracy will be compromised when they are measured with detectors with a nonuniform sub-pixel response such as HPC detectors. The smaller the spot is in comparison to the detector pixel size, the more severe the effect will be. In practice, one can mitigate this shortcoming conveniently by collecting true high-multiplicity data with a multi-axis goniometer[28], but at the cost of increased X-ray dose, and thus increased radiation damage[32] and experiment time. We have demonstrated that JUNGFRAU permits accurate measurement of photons regardless of where they land on the detector surface, which allows the user to obtain highly accurate data and thus achieve experimental phasing with minimum X-ray dose and reduced multiplicity (Fig. 4). Therefore, the JUNGFRAU detector holds great promise, especially for native-SAD phasing with X-rays in the range of 3–5 keV, where the calibration of HPC detectors is particularly challenging. Furthermore, the measurements can be carried out faster with high flux because JUNGFRAU is not count-rate limited. We demonstrated this unique combination of accuracy and speed in native-SAD experiments (Fig. 6a,b) with a rotation speed of 100° s^{-1}, a speed that was considered of no practical use in the past but now can be exploited for the development of novel data-collection strategies.

Time-resolved crystallography with Laue methods was made possible by third-generation high-energy synchrotron facilities[33]. However, Laue methods require large crystals and specialized beamlines. The emerging serial synchrotron crystallography (SSX) technique has introduced novel crystal-delivery techniques and automated data-collection methods with fast frame-rate detectors[34–37]. To further improve the efficiency of SSX methods and

the time resolution, one can increase the available flux density 100–1,000-fold through the use of wide-band-pass X-rays[38]. Then integrating detectors become indispensable. JUNGFRAU technology meets these challenges nicely and should allow the study of biologically relevant dynamics down to microsecond time scales in a pump-probe fashion at synchrotrons.

There are challenges to the implementation of JUNGFRAU at MX beamlines. 'Dark' runs (that is, without X-rays) are required to calculate pedestals for each gain and need to be included in the data-acquisition sequence with minimum overhead. The raw data need to be corrected and converted to photons before the data volume can be reduced by frame summation. This requires handling of high data rates (4 GB s^{-1} per 1 million pixels) for real-time data analysis. Researchers at the Paul Scherrer Institute are actively developing solutions to match the robustness and simplicity of operating HPC detectors. Such challenges are essentially the same for XFEL serial crystallography applications[39–41].

Current HPC detectors produce data of high quality for the majority of MX applications, but they have their limitations. The improvement in data accuracy and data-collection speed that we obtained with the JF1M detector is remarkable. The ultimate obtainable data quality from a given crystal depends on many factors, but it is evident that detectors like JUNGFRAU will be pivotal in helping scientists get close to this limit. We expect that detectors like JUNGFRAU will prompt the development of low-noise instruments in the next-generation MX beamlines to capitalize on the full potential of the next-generation synchrotron sources like diffraction-limited storage rings in the coming decade.

Online content

Any methods, additional references, Nature Research reporting summaries, source data, statements of data availability and associated accession codes are available at https://doi.org/10.1038/s41592-018-0143-7.

Received: 23 March 2018; Accepted: 25 July 2018;
Published online: 1 October 2018

References

1. Jaskolski, M., Dauter, Z. & Wlodawer, A. A brief history of macromolecular crystallography, illustrated by a family tree and its Nobel fruits. *FEBS. J.* **281**, 3985–4009 (2014).
2. Duke, E. M. H. & Johnson, L. N. Macromolecular crystallography at synchrotron radiation sources: current status and future developments. *Proc. R. Soc. Lond. A Math. Phys. Eng. Sci.* **466**, 3421–3452 (2010).
3. Gruner, S. M., Eikenberry, E. F. & Tate, M. W. in *International Tables for Crystallography* 2nd edn, Vol. F (eds Rossmann, M. G., Himmel, D. M. & Arnold, E.) 177–182 (International Union of Crystallography, Chester, UK, 2012).
4. von Seggern, H. Photostimulable x-ray storage phosphors: a review of present understanding. *Brazilian Journal of Physics* **29**, 254–268 (1999).
5. Howard, A. J. et al. The use of an imaging proportional counter in macromolecular crystallography. *J. Appl. Crystallogr.* **20**, 383–387 (1987).
6. Arndt, U. W. X-ray television area detectors. *Synchrotron Radiat. News* **3**, 17–22 (1990).
7. Gruner, S. M., Tate, M. W. & Eikenberry, E. F. Charge-coupled device area x-ray detectors. *Rev. Sci. Instrum.* **73**, 2815–2842 (2002).
8. Graafsma, H. in *Semiconductor Radiation Detection Systems* (ed Iniewski, K.) 217–236 (CRC Press, Boca Raton, FL, 2010).
9. Waterman, D. & Evans, G. Estimation of errors in diffraction data measured by CCD area detectors. *J. Appl. Crystallogr.* **43**, 1356–1371 (2010).
10. Dauter, Z. Data-collection strategies. *Acta Crystallogr. D Biol. Crystallogr.* **55**, 1703–1717 (1999).
11. Broennimann, Ch. et al. The PILATUS 1M detector. *J. Synchrotron. Radiat.* **13**, 120–130 (2006).
12. Mueller, M., Wang, M. & Schulze-Briese, C. Optimal fine φ-slicing for single-photon-counting pixel detectors. *Acta Crystallogr. D Biol. Crystallogr.* **68**, 42–56 (2012).
13. Dinapoli, R. et al. EIGER: next generation single photon counting detector for X-ray applications. *Nucl. Instrum. Methods. Phys. Res. A* **650**, 79–83 (2011).
14. Casanas, A. et al. EIGER detector: application in macromolecular crystallography. *Acta Crystallogr. D Struct. Biol.* **72**, 1036–1048 (2016).
15. Wojdyla, J. A. et al. Fast two-dimensional grid and transmission X-ray microscopy scanning methods for visualizing and characterizing protein crystals. *J. Appl. Crystallogr.* **49**, 944–952 (2016).
16. Diederichs, K. & Wang, M. in *Protein Crystallography: Methods and Protocols* (eds Wlodawer, A., Dauter, Z. & Jaskolski, M.) 239–272 (Humana Press, New York, 2017).
17. Ballabriga, R. et al. The Medipix3RX: a high resolution, zero dead-time pixel detector readout chip allowing spectroscopic imaging. *J. Instrum.* **8**, C02016 (2013).
18. Sobott, B. A. et al. Success and failure of dead-time models as applied to hybrid pixel detectors in high-flux applications. *J. Synchrotron. Radiat.* **20**, 347–354 (2013).
19. Loeliger, T. et al. in *2012 IEEE Nuclear Science Symposium and Medical Imaging Conference Record (NSS/MIC)* (ed Yu, B.) 610–615 (IEEE, New York, 2012).
20. Eriksson, M., van der Veen, J. F. & Quitmann, C. Diffraction-limited storage rings—a window to the science of tomorrow. *J. Synchrotron. Radiat.* **21**, 837–842 (2014).
21. Denes, P. & Schmitt, B. Pixel detectors for diffraction-limited storage rings. *J. Synchrotron. Radiat.* **21**, 1006–1010 (2014).
22. Graafsma, H., Becker, J. & Gruner, S. M. in *Synchrotron Light Sources and Free-Electron Lasers* (eds Jaeschke, E. et al.) 1029–1054 (Springer, Cham, 2016).
23. Tate, M. W. et al. A medium-format, mixed-mode pixel array detector for kilohertz X-ray imaging. *J. Phys. Conf. Ser.* **425**, 062004 (2013).
24. Mozzanica, A. et al. Characterization results of the JUNGFRAU full scale readout ASIC. *J. Instrum.* **11**, C02047 (2016).
25. Chapman, H. N. et al. Femtosecond X-ray protein nanocrystallography. *Nature* **470**, 73–77 (2011).
26. Redford, S. et al. First full dynamic range calibration of the JUNGFRAU photon detector. *J. Instrum.* **13**, C01027 (2018).
28. Weinert, T. et al. Fast native-SAD phasing for routine macromolecular structure determination. *Nat. Methods* **12**, 131–133 (2015).
32. Garman, E. F. Radiation damage in macromolecular crystallography: what is it and why should we care? *Acta Crystallogr. D Biol. Crystallogr.* **66**, 339–351 (2010).
33. Neutze, R. & Moffat, K. Time-resolved structural studies at synchrotrons and X-ray free electron lasers: opportunities and challenges. *Curr. Opin. Struct. Biol.* **22**, 651–659 (2012).
34. Gati, C. et al. Serial crystallography on in vivo grown microcrystals using synchrotron radiation. *IUCrJ* **1**, 87–94 (2014).
35. Weinert, T. et al. Serial millisecond crystallography for routine room-temperature structure determination at synchrotrons. *Nat. Commun.* **8**, 542 (2017).
36. Beyerlein, K. R. et al. Mix-and-diffuse serial synchrotron crystallography. *IUCrJ* **4**, 769–777 (2017).
37. Gruner, S. M. & Lattman, E. E. Biostructural science inspired by next-generation X-ray sources. *Annu. Rev. Biophys.* **44**, 33–51 (2015).
38. Meents, A. et al. Pink-beam serial crystallography. *Nat. Commun.* **8**, 1281 (2017).
39. Barty, A. et al. *Cheetah*: software for high-throughput reduction and analysis of serial femtosecond X-ray diffraction data. *J. Appl. Crystallogr.* **47**, 1118–1131 (2014).
40. Mariani, V. et al. *OnDA*: online data analysis and feedback for serial X-ray imaging. *J. Appl. Crystallogr.* **49**, 1073–1080 (2016).
41. Zeldin, O. B. et al. Data Exploration Toolkit for serial diffraction experiments. *Acta Crystallogr. D Biol. Crystallogr.* **71**, 352–356 (2015).

Acknowledgements

The project was funded by the Paul Scherrer Institute. We thank C. Tarnus, C. Schmitt, and S. Albrecht for the preparation of PepN crystals.

Author contributions

M.W., O.B., and B.S. conceived the research; S.R., A.M., and C.L.-C. built and calibrated the JF1M detector; A.M., D.B., and R.S. installed JF1M and E1M detectors at beamline X06SA; F.L., A.M., and E.P. developed diffraction-data collection software; L.V. and V.O. prepared samples; F.L., S.R., A.M., E.P., and M.W. collected data; F.L., S.R., K.N., D.O., G.T., E.F., K.D., and M.W. analyzed data; and F.L., S.R., O.B., and M.W. wrote the manuscript with contributions from all other authors.

Competing interests

The authors declare no competing interests.

Additional information

Supplementary information is available for this paper at https://doi.org/10.1038/s41592-018-0143-7.

Reprints and permissions information is available at www.nature.com/reprints.

Correspondence and requests for materials should be addressed to B.S. or M.W.

Publisher's note: Springer Nature remains neutral with regard to jurisdictional claims in published maps and institutional affiliations.

Methods

General experiment setup. Experiments were conducted at the X06SA protein crystallography undulator beamline, Swiss Light Source, at beam energies of 12.4 keV and 6 keV. The beam size was adjusted to $80\times80\,\mu m^2$ and the flux for a nonattenuated beam was 1.6×10^{12} photons (ph)/s and 2.7×10^{11} ph/s for 12.4 and 6 keV, respectively. For 12.4-keV measurements we used the default beamline settings, whereas for 6 keV we detuned the monochromator by 0.002° to remove higher harmonics. The beamstop was placed 7 mm from the sample, which shadowed reflections with resolutions less than 10 Å for 12.4-keV X-rays. The beamline was equipped with a motorized stage that allowed movement of the JUNGFRAU and EIGER detectors in three directions. Sample-to-detector distance could be changed in the 40–120 mm range, and the two perpendicular directions could be set within 20 mm from the detector center. The motor resolution was 2.5 µm. Crystal centering and EIGER data collection were controlled with DA+ software[42]. The JUNGFRAU data collection was carried out with customized programs.

JF1M detector characteristics. The unique feature of the JUNGFRAU detector is its dynamic gain-switching, with three gain levels accommodating both single-photon sensitivity and high dynamic range. The JUNGFRAU detector is modular, and each module has an active area of $4\times8\,cm^2$ with eight application-specific integrated circuits (ASICs) and contains ~500,000 pixels of 75-µm pitch. The sensor geometry is identical to that of EIGER. Modules are independent in terms of readout; each has a dedicated 10 GB/s Ethernet link and can be arranged into various geometric shapes. Currently silicon of 320-µm thickness is used for the JUNGFRAU sensor. A thicker sensor, such as the 450-µm-thick sensor of EIGER, could also be used.

The JUNGFRAU system used in this experiment consisted of two modules forming a 1-million-pixel system (JF1M). The gap between the modules, insensitive to X-rays, was estimated at ~2.7 mm (36 pixels). The system was operated with an 880-µs frame time (1,136 Hz) and 840-µs integration time (i.e., a duty cycle of 95%). This almost continuous mode is very different from the pulse mode used for XFEL applications. The integration time and the frame rate were determined by detector characteristics coupled with the desire to achieve as high a duty cycle as possible. To limit the integration of the leakage current, we used the present maximum frame rate of 1,136 Hz, corresponding to a period of 880 µs. A window of 40 µs is required between the end of integration and the start of readout to allow charge to move through the chip; this leaves an integration time of 840 µs. The previous frame is then read out during the integration of the next frame. To further reduce the leakage current, we cooled the detector to −12 °C. Other parameters, such as the internal ASIC voltages, sensor bias voltage, and timings, were standard as also used in XFELs. We used a dedicated computer to control the detector and to store frames during data collection. The frame rate (1,136 Hz) and frame size (1 million pixels in 16-bit) required a wide bandwidth of 2.3 GB/s to prevent frame loss.

The ASIC of JUNGFRAU is designed to keep the readout noise below Poisson statistics and to have single-photon sensitivity at energies as low as 2 keV. The readout noise is estimated as 200 electrons for the high gain with an integration time of 840 µs. When the detector is operated at an XFEL with an integration time of 10 µs, the noise is reduced to 70 electrons.

The maximum number of counts is determined by the charge range of the low gain. Because the induced charge from a single photon is proportional to its energy, the dynamic range is effectively doubled at 6 keV compared with that at 12 keV. When the detector is operated at a 1.1-kHz frame rate, the dynamic range is about 12 and 25 Mcps $pixel^{-1}$ (2,100 and 4,400 Mcps mm^{-2}) at 12 and 6 keV, respectively, and is roughly doubled at the foreseen operation frame rate of 2.3 kHz.

JUNGFRAU data format and image processing. The result of each JUNGFRAU measurement is a raw image. For each pixel, the gain level (2-bit) and digitized accumulated charge (14-bit) are recorded. For conversion of raw signal to photon energy, six constants are needed per pixel: for each of the three gain levels, one needs to know the amplification factor (i.e., the ratio of arbitrary detector charge units and energy) and the pedestal (i.e., the offset corresponding to the pixel's dark output).

Gain values are assumed to be invariant with experimental conditions and were measured for the JF1M previously[26]. The achieved accuracy of the gain calibration is at about 1% currently[43]. The pedestal, in contrast, depends strongly on experimental conditions, especially the integration time and the sensor temperature. Therefore, we obtained dedicated dark measurements before measurement of every dataset with JF1M, consisting of 5,000 frames in high gain (1,136 Hz), 1,000 in medium gain (500 Hz), and 1,000 in low gain (200 Hz). We observed pedestal drift immediately after the detector began recording, related to the changes in temperature and operation mode for this particularly long integration time, and introduced a delay of 10 s between detector start and shutter opening to address this. Frames measured during this period were used to dynamically track the pedestal but were not used for data processing. Currently, such a procedure introduces an ~60-s delay for an experiment. It is expected that much shorter and less frequent measurement would be sufficient, and optimization for efficiency is under study.

We applied pedestal subtraction and gain conversion on raw images after data collection. We converted the energy measured per pixel to a photon count by dividing by the incoming photon energy. We applied geometric corrections to account for the ~36-pixel gap between the modules, and the multi-size pixels between the ASICs. Finally, we carried out an optional frame summation. Because the conversion of analog-to-digital converter units (ADUs) to photon counts does not yield integers, and because floating point values are not supported by common crystallography data-processing packages, we rounded these values to the nearest integer; final images were saved in CBF format[44]. Pixels that saturated the highest possible ADU count at the lowest gain were marked as overloads.

E1M detector. We obtained comparative data with an E1M detector (Dectris Ltd.). The detector consists of two modules, each with ~500,000 pixels of 75-µm pitch, meaning the format is directly comparable to that of the JF1M detector used in this study. The sensor thickness is 450 µm. Images were saved in HDF5 format.

Protein crystal preparation. Lysozyme was dissolved at 50 mg/ml in 50 mM sodium acetate, pH 4.5, and crystallized in 5% PEG MME 5000, 2 M NaCl, 50 mM sodium acetate, pH 4.5, 25% ethylene glycol. Thaumatin was suspended at 50 mg/ml in water and crystallized in 24% sodium potassium tartrate, 100 mM Bis-Tris propane, pH 6.5. Both lysozyme and thaumatin were obtained from Sigma-Aldrich. PepN was purified and crystallized with inhibitor I1 according to a published protocol[45].

X-ray data collection. *Low-noise performance.* A large thaumatin crystal (Thau1; $480\times240\times180\,\mu m^3$) was measured at 12.4 keV with a flux of 3.5×10^9 ph/s (0.25% beam transmission). The datasets with full rotation (360°) were measured at a rotation speed of 50° s^{-1} with both JF1M and E1M detectors. The accumulated dose was about 0.6 kGy per dataset[46]. The crystal was kept on the goniometer while detectors were exchanged, so both measurements were made with the same position of the crystal and same X-ray beam conditions. The JF1M and E1M detectors were positioned approximately 60 mm from the sample and operated at a 1.136-kHz frame rate and 500 Hz, respectively.

Dynamic range study. A thaumatin crystal (Thau2) with a size of $80\times80\times80\,\mu m^3$, matching the beam size, was measured at 6 keV with JF1M positioned approximately 40 mm from the crystal. Four 360° datasets were measured with four settings: (1) 100° s^{-1} rotation speed and 100% beam transmission, (2) 50° s^{-1} and 50% transmission, (3) 20° s^{-1} and 20% transmission, and (4) 1° s^{-1} and 1% transmission. Because we intended to compare the intensities from settings (1) and (4), we measured the attenuation factor for setting (4) with a photodiode, and found that the precise transmission was 1.16%. Therefore, intensities of data with 1% transmission reported in Fig. 3c,d were divided by a factor of 1.16.

Frames were summed by 2 in the case of 50% transmission, by 5 in the case of 20% transmission, and by 100 in the case of 1% transmission. This means all datasets had the same X-ray dose and the same angular increment per summed image. The total dose accumulated through the experiment was estimated as less than 0.5 MGy, well below the damaging dose limit for cryo-cooled crystals.

Sub-pixel uniformity study. Measurements were carried out with both JF1M and E1M detectors operated with the same frame rate of 1.136 kHz and positioned 45 mm from the crystal. Two settings were used for the E1M: one with the default 50% threshold (E1M-50), and the other with 60% (E1M-60). The integration times of JF1M and E1M were 840 µs and 877 µs, corresponding to duty cycles of 95.5% and 99.7%, respectively. A large thaumatin crystal (Thau3) of about $360\times240\times240\,\mu m^3$ was measured at 6 keV with 15% beam transmission (flux of 2.5×10^{10} ph/s). The same crystal volume was illuminated with the same X-ray beam through the entire experiment.

All diffraction data were collected with a rotation speed of 10° s^{-1}, that is, a step of 0.0088° in 0.00088 s. Five 360° datasets were measured for each detector. We carried out the first two runs with the detector in an initial position, the third with the detector shifted by 25 µm (1/3 pixel) in both *x* and *y* directions from the initial position, the fourth with the detector shifted by 50 µm (2/3 pixel) in both *x* and *y* directions, and final one with the detector shifted by 225 µm (3 pixels) in both *x* and *y* directions relative to the initial position. Only results of the first three experiments are presented. The total dose accumulated through the experiment was estimated as 1 MGy. For data processing, images from both detectors were summed by ten, so one frame corresponds to a 0.088° rotation.

Fast native-SAD phasing. For native SAD at 6 keV X-ray energy, we used a beam size of $80\times80\,\mu m^2$ and the full flux of 2.7×10^{11} ph/s. A thaumatin crystal with a size matching the beam size (Thau2; $80\times80\times80\,\mu m^3$) was measured for a 360° angular range at 100° s^{-1} rotation speed. The frames with 0.088° angular increment were used for data processing directly, without summing. The same setup at 6 keV for a PepN crystal of $100\times80\times80\,\mu m^3$ was used to measure a 720° angular range at a rotation speed of 10° s^{-1}. Ten frames were summed to make one image covering a 0.088° rotation width.

For native SAD at 12.4 keV, a lysozyme crystal of $80\times80\times80\,\mu m^3$ was used. The lysozyme dataset was measured with 100° s^{-1} rotation speed and 100% beam transmission (1.6×10^{12} ph/s).

X-ray data processing, structure determination, and refinement. MX data quality is dependent on phi-slicing[12,14], and in principle a slower rotation speed allows for finer slicing at a given detector frame rate, which could result in a bias toward slower rotation speeds (up to the point where data-processing software can correctly account for the extremely weak signal and low background). Therefore, before data processing, we carried out frame summation to ensure that images obtained at various rotation speeds corresponded to a similar rotation angle (0.088° for 1.136 kHz and 0.100° for 1.000 kHz).

Frames were processed with XDS[47] software with standard settings. To improve position refinement for the pixel map calculation, we used the segment refinement feature of XDS to account for imprecisions in module positions and the gap size in JF1M and E1M. To allow a direct comparison of intensities for the dynamic range and low-noise performance experiments, we fixed scaling factors for integration in XDS at 1.0. We divided intensities calculated in the XDS_ASCII.HKL by the Lorenz-polarization correction factor, to recover the total photon count of a reflection for presentation in Fig. 2c.

The calculation of data-quality indicators (R_{merge}, R_{meas}, and $\langle I/\sigma \rangle$) was performed on the basis of XDS and XSCALE outputs using custom Python scripts for plotting in finer-resolution shells. In the low-noise performance experiment, the normalization of intensity was calculated with the ratio of the duty cycles and the ratio of the absorptions of the Si sensor at 2θ of 32° (Fig. 2c). I/σ was normalized with the square root of the ratios (Fig. 2d). The duty cycle was 95% and 99.7% and the sensor thickness was 320 µm and 450 µm for JF1M and E1M, respectively.

Experimental phasing with native SAD was carried out with SHELXC/D/E[30] via HKL2MAP GUI[48] or with the CRANK2 pipeline[31]. The mean peak height for anomalous data $\langle S_{anom} \rangle$ was calculated with ANODE[49]. The structures were refined with phenix.refine[50] and deposited in the Protein Data Bank (see "Data availability").

Sub-pixel uniformity characterization. To explore the systematic errors of the detector on the sub-pixel level, we grouped all the reflections according to where they impinged relative to a pixel center. In this task we benefited from the fact that XDS provides the predicted reflection center to a precision of 1/10 of a pixel. For each reflection we considered only the fractional part of its position in pixel units, ignoring its integer part. For example, if a spot was predicted to fall at $x = 450.1$ pixel and $y = 363.5$ pixel, we considered its 'in-pixel position' as $x = 1$, $y = 5$. Because in XDS the coordinate system in-pixel position $x = 0$, $y = 0$ corresponds to the center of a pixel, we shifted the positions by half a pixel to put the origin of the coordinate system at a corner.

To quantify such spatial effects, we first calculate the deviation from the mean for each observation:

$$\Delta = \sqrt{\frac{n}{n-1}}\ (I_{obs} - \overline{I_{obs}}) \tag{1}$$

where n is multiplicity, I_{obs} is the measured intensity, and $\overline{I_{obs}}$ is the mean intensity for all symmetry equivalent reflections (including the one in question). The extra term $\sqrt{n\ /\ (n-1)}$ corrects for underestimation of the difference between the observation and the mean[51]. R_{meas} is then simply

$$R_{meas} = \frac{\sum_{hkl} \sum_n |\Delta|}{\sum_{hkl} \sum_n \overline{I_{obs}}} \tag{2}$$

where n is the multiplicity. Reflections that were observed only once are ignored in the summation.

Next we bin all reflections according to their in-pixel position, and for each position x,y we calculate

$$\Delta_{x,y} = \sum_{hkl} \sum_n \Delta \tag{3}$$

where n is the number of reflections that fall into a particular x,y in-pixel position. To allow comparison between in-pixel positions, $\Delta_{x,y}$ can be also normalized similarly to R factors:

$$\Delta^{norm}_{x,y} = \frac{\Delta_{x,y}}{\sum_{hkl} \sum_n \overline{I_{obs}}} \tag{4}$$

Because $\Delta^{norm}_{x,y}$ is calculated without the absolute value of $\Delta_{x,y}$ being taken before averaging, random differences in intensity measurements should cancel out—a value close to zero of $\Delta^{norm}_{x,y}$ should indicate that there is no systematic error introduced at in-pixel position x,y. However, if reflections in a particular bin are systematically larger or smaller than the ones in other bins, $\Delta^{norm}_{x,y}$ should indicate it by a positive or negative value, respectively. $\Delta^{norm}_{x,y}$ values for each in-pixel position can then be presented on a map that indicates the degree of the nonuniformity across 1 pixel. Pixel maps calculated with low-resolution reflections ($d > 10$ Å) are presented in Fig. 5a–c.

With the value of $\Delta_{x,y}$ known, one can calculate the effect that charge sharing has on the R factor value, by calculating the mean of the absolute values of $\Delta_{x,y}$:

$$R_{pxl} = \frac{\sum_{x,y} |\Delta_{x,y}|}{\sum_{hkl} \sum_n \overline{I_{obs}}} \tag{5}$$

where n is the number of all reflections with multiplicity of at least two. Because $|a| + |b| \geq |a + b|$, R_{meas} is an upper limit for R_{pxl}, and comparison of the two values can indicate the share of systematic errors due to sub-pixel nonuniformity in relation to the total uncertainty.

For calculations we apply a standard cutoff for reflection intensities of $I > -3\sigma$. Because we are interested in systematic deviations of reflection intensities, we also include misfits, marked in XDS_ASCII.HKL with negative σ values, in all statistics calculations presented in Fig. 5d–f (R_{pxl} and R_{meas}).

Photon count-rate estimation. The peak photon rate for a reflection observation was approximated as the following:

$$\text{Rate} = \frac{\text{Max } C}{(0.075 \text{ mm})^2} \frac{\nu}{\Delta\phi} \tag{6}$$

where Max C is the highest count observed in a single pixel from a single frame for a particular reflection (column MAXC in INTEGRATE.HKL from XDS), ν is the rotation speed in degrees per second, $\Delta\phi$ is the rotation range of a single image in degrees, and 0.075 mm is the pixel pitch. This number is only the lower estimation of the peak rate, because while a crystal rotates, the intensity of a reflection varies according to its rocking curve, especially if $\Delta\phi$ is larger than the mosaicity (as in our case). However, if one compares two datasets collected with the same $\Delta\phi$, the incoming photon rate should be similar in both. The spread in observed values might come from the different spread of counts inside a peak (charge sharing).

In Fig. 3d we present correlations of peak rates of two JF1M datasets collected on the same crystal at 1° s^{-1} and 100° s^{-1} rotation speeds with corresponding beam transmissions of 1% and 100% (see above for exact experimental details). To ensure that equivalent $\Delta\phi$ frame summation was performed on the slower dataset, for the correlation plot, we chose only reflections with identical Miller indices from both datasets, and we applied no symmetry equivalence. In this way, peak rates calculated in 1° s^{-1} JF1M data, multiplied by 100, are an approximation of the 'true' rates for 100° s^{-1} data. These rates are then compared with the measured rate values in 100° s^{-1} data.

For reference, we calculate peak rate values using a theoretical model for a paralyzable counter, where the relation between true count rate I_0 and observed count rate I is given as

$$I = I_0 e^{-I_0 \tau} \tag{7}$$

where τ is an energy-dependent sensor dead time. The τ value used in Fig. 3d was taken as 280 ns, which is an experimental value determined for 6-keV photons for the PSI manufactured EIGER[52].

Reporting Summary. Further information on research design is available in the Nature Research Reporting Summary linked to this article.

Code availability. Custom computer code for pixel maps and R_{pxl} calculations are available at https://github.com/fleon-psi/JF_analysis_scripts.

Data availability

All diffraction data have been deposited in the figshare depository and are accessible at https://doi.org/10.6084/m9.figshare.6087368. Diffraction data and refined models for native-SAD structures have been deposited in the Protein Data Bank as PDB 6G89 (thaumatin), 6G8A (lysozyme), and 6G8B (PepN). Source data for Figs. 2–6 are available online.

References

27. Liu, Q. et al. Structures from anomalous diffraction of native biological macromolecules. *Science* **336**, 1033–1037 (2012).
29. Terwilliger, T. C. et al. Can I solve my structure by SAD phasing? Anomalous signal in SAD phasing. *Acta Crystallogr. D Struct. Biol.* **72**, 346–358 (2016).
30. Sheldrick, G. M. Experimental phasing with SHELXC/D/E: combining chain tracing with density modification. *Acta Crystallogr. D Biol. Crystallogr.* **66**, 479–485 (2010).
31. Skubák, P. & Pannu, N. S. Automatic protein structure solution from weak X-ray data. *Nat. Commun.* **4**, 2777 (2013).
42. Wojdyla, J. A. et al. DA+ data acquisition and analysis software at the Swiss Light Source macromolecular crystallography beamlines. *J. Synchrotron. Radiat.* **25**, 293–303 (2018).
43. Redford, S. et al. Calibration status and plans for the charge integrating JUNGFRAU pixel detector for SwissFEL. *J. Instrum.* **11**, C11013 (2016).

44. Bernstein, H. J. & Hammersley, A. P. in *International Tables for Crystallography* Vol. G (eds Hall, S. R. & McMahon, B.) 37–43 (International Union of Crystallography, Chester, UK, 2006).
45. Peng, G. et al. Insight into the remarkable affinity and selectivity of the aminobenzosuberone scaffold for the M1 aminopeptidases family based on structure analysis. *Proteins* **85**, 1413–1421 (2017).
46. Paithankar, K. S., Owen, R. L. & Garman, E. F. Absorbed dose calculations for macromolecular crystals: improvements to RADDOSE. *J. Synchrotron. Radiat.* **16**, 152–162 (2009).
47. Kabsch, W. XDS. *Acta Crystallogr. D Biol. Crystallogr.* **66**, 125–132 (2010).
48. Pape, T. & Schneider, T. R. HKL2MAP: a graphical user interface for macromolecular phasing withSHELXprograms. *J. Appl. Crystallogr.* **37**, 843–844 (2004).
49. Thorn, A. & Sheldrick, G. M. ANODE: anomalous and heavy-atom density calculation. *J. Appl. Crystallogr.* **44**, 1285–1287 (2011).
50. Afonine, P. V. et al. Towards automated crystallographic structure refinement with *phenix.refine*. *Acta Crystallogr. D Biol. Crystallogr.* **68**, 352–367 (2012).
51. Diederichs, K. & Karplus, P. A. Improved R-factors for diffraction data analysis in macromolecular crystallography. *Nat. Struct. Biol.* **4**, 269–275 (1997).
52. Johnson, I. et al. Eiger: a single-photon counting x-ray detector. *J. Instrum.* **9**, C05032 (2014).

nature research

Corresponding author(s): Meitian Wang, Bernd Schmitt

Reporting Summary

Nature Research wishes to improve the reproducibility of the work that we publish. This form provides structure for consistency and transparency in reporting. For further information on Nature Research policies, see Authors & Referees and the Editorial Policy Checklist.

Statistical parameters

When statistical analyses are reported, confirm that the following items are present in the relevant location (e.g. figure legend, table legend, main text, or Methods section).

n/a	Confirmed	
☒	☐	The exact sample size (*n*) for each experimental group/condition, given as a discrete number and unit of measurement
☒	☐	An indication of whether measurements were taken from distinct samples or whether the same sample was measured repeatedly
☒	☐	The statistical test(s) used AND whether they are one- or two-sided *Only common tests should be described solely by name; describe more complex techniques in the Methods section.*
☒	☐	A description of all covariates tested
☒	☐	A description of any assumptions or corrections, such as tests of normality and adjustment for multiple comparisons
☐	☒	A full description of the statistics including central tendency (e.g. means) or other basic estimates (e.g. regression coefficient) AND variation (e.g. standard deviation) or associated estimates of uncertainty (e.g. confidence intervals)
☒	☐	For null hypothesis testing, the test statistic (e.g. *F*, *t*, *r*) with confidence intervals, effect sizes, degrees of freedom and *P* value noted *Give P values as exact values whenever suitable.*
☒	☐	For Bayesian analysis, information on the choice of priors and Markov chain Monte Carlo settings
☒	☐	For hierarchical and complex designs, identification of the appropriate level for tests and full reporting of outcomes
☒	☐	Estimates of effect sizes (e.g. Cohen's *d*, Pearson's *r*), indicating how they were calculated
☒	☐	Clearly defined error bars *State explicitly what error bars represent (e.g. SD, SE, CI)*

Our web collection on statistics for biologists may be useful.

Software and code

Policy information about availability of computer code

Data collection	DA+
Data analysis	XDS/XSCALE 2017 version, SHELX 2016/1 version, CCP4 7.0, CRANK2, Phenix 1.12rc2

For manuscripts utilizing custom algorithms or software that are central to the research but not yet described in published literature, software must be made available to editors/reviewers upon request. We strongly encourage code deposition in a community repository (e.g. GitHub). See the Nature Research guidelines for submitting code & software for further information.

Data

Policy information about availability of data

All manuscripts must include a data availability statement. This statement should provide the following information, where applicable:

- Accession codes, unique identifiers, or web links for publicly available datasets
- A list of figures that have associated raw data
- A description of any restrictions on data availability

All diffraction data have been deposited in figshare depository and are accessible at doi:10.6084/m9.figshare.6087368. Diffraction data and refined models for native-SAD structures have been deposited in the Protein Data Bank under PDB identifiers 6G89 (thaumatin), 6G8A (lysozyme), and 6G8B (PepN).

Field-specific reporting

Please select the best fit for your research. If you are not sure, read the appropriate sections before making your selection.

☒ Life sciences ☐ Behavioural & social sciences ☐ Ecological, evolutionary & environmental sciences

For a reference copy of the document with all sections, see nature.com/authors/policies/ReportingSummary-flat.pdf

Life sciences study design

All studies must disclose on these points even when the disclosure is negative.

Sample size	Any well diffracting crystals are suitable for detector characterizations. Sample size is not relevant for this study.
Data exclusions	No data were excluded from the analyses.
Replication	Three native-SAD data sets from different systems were reported.
Randomization	All crystals were systematically screened and selected for this study. Randomization is not relevant for this study.
Blinding	Blinding is not relevant for macromolecular crystallography.

Reporting for specific materials, systems and methods

Materials & experimental systems

n/a	Involved in the study
☒	☐ Unique biological materials
☒	☐ Antibodies
☒	☐ Eukaryotic cell lines
☒	☐ Palaeontology
☒	☐ Animals and other organisms
☒	☐ Human research participants

Methods

n/a	Involved in the study
☒	☐ ChIP-seq
☒	☐ Flow cytometry
☒	☐ MRI-based neuroimaging